Heat flux prediction for hypersonic flows using a stabilized formulation

David Codoni[1] · Ahmed Bayram[1] · Manoj Rajanna[2] · Craig Johansen[1] · Ming-Chen Hsu[2] · Yuri Bazilevs[3] ·
Artem Korobenko[1]

Abstract

This work focuses on the heat flux prediction in hypersonic flow regimes using the finite-element based Streamline-Upwind
Petrov–Galerkin formulation enhanced with a discontinuity-capturing operator and weak enforcement of the Dirichlet boundary condition. The numerical formulation is validated on several benchmark cases including Mach 14 compression corner at 15° and 24°, 2D Mach 17 cylinder and 3D Mars Pathfinder re-entry vehicle at Mach 14. The numerical results are in very good agreement with the experiments or data available in the literature, showing the robustness of the numerical framework. Moreover, the newly proposed weak imposition of the no-slip boundary condition at the surface shows great potential for near-wall modeling of high-speed compressible flows.

Keywords Hypersonic flows · Stabilized methods · Heat transfer · Finite elements · Weak boundary conditions

1 Introduction

One of the main challenges faced by engineers during the design process of a hypersonic aircraft is the severe aerodynamic heating it experiences throughout its mission [40]. In the hypersonic regime, the interaction of air friction and complex flow phenomena, such as shock–shock and shock wave-boundary layer interactions, generates a significant amount of heat and conventional methods to provide a single-point temperature and heat flux values is insufficient. In recent years, the progress has been made in advancing numerical methods for aerothermal analysis of hypersonic flows [12, 29–32] and the accurate heat flux prediction was identified as one of the key issues [25]. In [23–25] the authors conducted an assessment of the classic finite volumes techniques, showing the sensitivity of these methods to the mesh topology and inviscid flux functions in predicting heat transfer. The finite element based methods, on the other hand, do not exhibit these behaviour and can be considered as a

promising alternative for hypersonic flows modeling [7, 8]. While both methods can handle very complex geometries [43], the finite elements allows a simplified implementation of boundary conditions and higher-order accuracy, which are nontrivial challenges in the context of finite volume methods [11].

Significant progress has been made over the past decades in the stabilized methods based on the Streamline-Upwind Petrov–Galerkin (SUPG) formulation [5, 17, 44, 45] enhanced with a discontinuity capturing (DC) operator [18, 27, 46–48, 52]. These methods have been successfully applied to various compressible flow problems with traditional linear finite elements and in a context of isogeometric analysis (IGA) with non-uniform rational B-splines (NURBS). This includes simulations of a delta-wing [49, 50], aircrafts and rotorcrafts [34, 35, 50, 51, 55], missiles [39], gas turbines [4, 26, 54], spacecraft parachutes [21, 41], re-entry vehicles in hypersonic regime [9] and more recently the hypersonic flows in thermo-chemical non-equilibrium [10, 22].

The selection of the stabilization parameters, including the element length calculation, estimation of the constants, plays a crucial role and require a careful balance between accuracy and stability [13]. The review of the stabilization parameters is outside of the scope of this article and the interested reader is referred to a review article on the stabilized methods for compressible flows in [19] and recent paper on stabilization and discontinuity-capturing parameters in [42].

✉ Artem Korobenko
artem.korobenko@ucalgary.ca

1 Department of Mechanical and Manufacturing Engineering, University of Calgary, Calgary, AB T2L1Y6, Canada

2 Department of Mechanical Engineering, Iowa State University, Ames, IA 50011, USA

3 School of Engineering, Brown University, Providence, RI 02912, USA

The current work extends the formulation presented in [9] for hypersonic flows by introducing the weakly enforced Dirichlet boundary conditions [4, 54]. The focus of this study is to examine the performance of weakly imposed essential boundary conditions in predicting heat flux in the hypersonic regime. The rest of the article is structured as follows. The mathematical formulation is described in Sect. 2, followed by the numerical tests presented in Sect. 3. The conclusion and future work are discussed in Sect. 4.

2 Numerical formulation

The set of compressible Navier–Stokes equations in conservative form can be written as

$$\partial_t \mathbf{U} + \nabla \cdot \mathbf{F} + \mathbf{S} = \mathbf{0}, \tag{1}$$

where ∂_t represents the Eulerian time derivative and the vector of the conservative variables $\mathbf{U}$, source term $\mathbf{S}$, flux vector $\mathbf{F}$, which consists of convective flux $\mathbf{F}^{conv}$, pressure flux $\mathbf{F}^p$ and diffusive flux $\mathbf{F}^{diff}$, are given by

$$\mathbf{U} = \begin{vmatrix} \rho \\ \rho\mathbf{u} \\ \rho\left(e + \mathbf{u}\cdot\mathbf{u}/2\right) \end{vmatrix} \quad \mathbf{F}^{conv} = \mathbf{U}\otimes\mathbf{u} \quad \mathbf{F}_p = \begin{vmatrix} \mathbf{0}^T \\ p\mathbf{I} \\ \mathbf{u}^T p \end{vmatrix}$$

$$\mathbf{F}^{diff} = -\begin{vmatrix} \mathbf{0}^T \\ \boldsymbol{\tau} \\ \mathbf{u}^T\boldsymbol{\tau} + \kappa\left(\nabla T\right)^T \end{vmatrix} \quad \mathbf{S} = \begin{vmatrix} 0 \\ \rho\mathbf{b} \\ \rho\left(\mathbf{b}\cdot\mathbf{u} + r\right) \end{vmatrix} \tag{2}$$

In Eq. 2, ρ is the density, $\mathbf{u}$ is the velocity vector, T is the thermodynamic temperature, p is the pressure, $\mathbf{b}$ is a body force, r is a heat source/sink, $e = c_v T$ is the internal energy, c_v is the specific heat at constant volume, κ is the thermal conductivity, $\mathbf{I}$ is the identity tensor, and $\boldsymbol{\tau}$ is the second order viscous stress tensor defined as

$$\boldsymbol{\tau} = \lambda\nabla\cdot\mathbf{u} + \mu\left((\nabla\mathbf{u}) + (\nabla\mathbf{u})^T\right), \tag{3}$$

where λ is the bulk viscosity and μ is the dynamic viscosity. We also assume the equation of state for the ideal gas.

Together with Eq. 1, the Dirichlet boundary conditions $\mathbf{U} = \mathbf{U_G}$ on a domain boundary Γ_g are considered, where $\mathbf{U_G} = [\rho,\ \rho\mathbf{g}^T,\ \rho c_v\left(T_w + \mathbf{g}\cdot\mathbf{g}/2\right)]^T$, with $\mathbf{g}$ being the prescribed velocity vector, and T_w being the prescribed wall temperature.

Equation 1 can be also written in a quasi-linear form using a set of pressure-primitive variables $\mathbf{Y} = [p,\ \mathbf{u}^T,\ T]^T$ as

$$\mathbf{A}_0\,\partial_t\mathbf{Y} + \mathbf{A}\,\nabla\cdot\mathbf{Y} = \mathbf{0}, \tag{4}$$

where $\mathbf{A}_0 = \nabla_\mathbf{Y}\mathbf{U}$ is a transformation matrix from conservative to pressure-primitive variables, and the Jacobian matrix

$\mathbf{A} = \mathbf{A}^{conv} + \mathbf{A}^p + \mathbf{A}^{diff} = \nabla_\mathbf{U}\mathbf{F}\mathbf{A}_0$. In Eq. 4, the source term $\mathbf{S}$ is assumed to be zero. In this form, the Dirichlet boundary conditions become $\mathbf{Y} = \mathbf{Y_G}$, where $\mathbf{Y_G} = [p,\ \mathbf{u}^T,\ T]^T$. The reader is referred to the appendix of [9] for the explicit expressions of the matrices appearing in the quasi-linear form, and [14] for comparison of different set of variables.

The semi-discrete variational form is obtained by applying the method of weighted residuals to Eq. 4 with the integration by parts performed on the pressure and diffusive fluxes. To stabilize the formulation the SUPG term is added on the interior of each element [9, 54]. Moreover, due to the presence of strong shock waves in the flow, additional dissipation is added through the discontinuity capturing (DC) operator [1, 4, 9, 10, 27, 28, 54]. The final semi-discrete weak form can be written as

$$\int_\Omega \mathbf{W}^h \cdot \left(\mathbf{A}_0\cdot\mathbf{Y}^h_{,t} + \mathbf{A}^{conv}_i\cdot\mathbf{Y}^h_{,i}\right)d\Omega$$

$$-\int_\Omega \mathbf{W}^h_{,i}\cdot\left(\mathbf{A}^p_i\cdot\mathbf{Y}^h - \mathbf{K}_{ij}\cdot\mathbf{Y}^h_{,j}\right)d\Omega$$

$$+\sum_e^{N_{el}}\int_{\Omega_e}\mathbf{W}^h_{,i}\mathbf{A}^T_i\boldsymbol{\tau}_{SUPG}\mathbf{Res}\,d\Omega$$

$$+\sum_e^{N_{el}}\int_{\Omega_e}\mathbf{W}^h_{,i}\mathbf{K}_{DC}\mathbf{Y}^h_i\,d\Omega$$

$$+\int_{\Gamma_h}\mathbf{W}^h\cdot\left(\mathbf{A}^p_i\cdot\mathbf{Y}^h - \mathbf{K}_{ij}\cdot\mathbf{Y}^h_{,j}\right)n_i\,d\Gamma$$

$$\int_{\Gamma_g}\mathbf{W}^h\cdot\left(\mathbf{A}^p_i\cdot\mathbf{Y}^h\right)n_i\,d\Gamma - \int_{\Gamma_g}\mathbf{W}^h\cdot\left(\mathbf{K}_{ij}\cdot\mathbf{Y}^h_{,j}\right)n_i\,d\Gamma$$

$$-\int_{\Gamma_g}\left(\mathbf{K}_{ij}\cdot\mathbf{W}^h_{,j}\right)\cdot\left(\mathbf{Y}^h - \mathbf{Y}^h_\mathbf{G}\right)n_i\,d\Gamma$$

$$+\int_{\Gamma_g}\mathbf{W}^h\cdot\boldsymbol{\tau}_B\cdot\left(\mathbf{Y}^h - \mathbf{Y}^h_\mathbf{G}\right)d\Gamma$$

$$-\int_{\Gamma_g}\mathbf{W}^h\cdot\{\hat{\mathbf{A}}_\mathbf{n}\}_-\cdot\left(\mathbf{U}(\mathbf{Y}^h) - \mathbf{U}(\mathbf{Y}^h_\mathbf{G})\right)d\Gamma$$

$$= 0, \tag{5}$$

where $i, j = 1\ldots n_d$ are the indexes for the spatial dimension, d is the number of space dimensions, $\Omega \subset \mathbb{R}^d$ is the volumetric domain which is descritized using linear finite elements as $\Omega = \cup_{e=1}^{n_{el}}\Omega_e$. The natural boundary conditions are enforced on $\Gamma_h \in \Gamma$ and the essential boundary conditions are enforced on $\Gamma_g \in \Gamma$. n_i is the ith component of outward unit surface normal vector $\mathbf{n}$. In Eq. 5, $\mathbf{Y}^h$ and $\mathbf{W}^h$ are the solution and test functions from the finite dimensional spaces $\mathbf{S}^h$ and $\mathbf{V}^h$ respectively. $\mathbf{Res}$ is the strong-form residual. $\boldsymbol{\tau}_{SUPG}$ is the stabilization matrix in pressure-based primitive variables [9]

$$\boldsymbol{\tau}_{SUPG}$$

$$= \mathbf{A}_0^{-1} \left(\frac{4}{\Delta t^2} \mathbf{I} + G_{ij} \mathbf{A}_i \mathbf{A}_j + C_I \ G_{ij} G_{kl} \mathbf{K}_{ik} \mathbf{K}_{jl} \right)^{-\frac{1}{2}} \quad (6)$$

where Δt is the time step size, C_I is a positive constant derived from an appropriate element-wise inverse estimate ($C_I = 3$ for all cases presented in this work) and G_{ij} are the components of the element metric tensor. $\mathbf{K}_{DC}$ is a diagonal diffusivity matrix for discontinuity capturing

$$\mathbf{K}_{DC} = C_{DC} \left(\frac{\mathbf{Res}^{\mathrm{T}} \tilde{\mathbf{A}}_0^{-1} \mathbf{Res}}{G_{ij} \mathbf{U}_{,i}^{\mathrm{T}} \tilde{\mathbf{A}}_0^{-1} \mathbf{U}_{,j}} \right)^{\frac{1}{2}} \mathbf{A}_0, \quad (7)$$

where C_{DC} is a positive constant ($C_{DC} = 1$ for all cases presented in this work), and $\tilde{\mathbf{A}}_0^{-1}$ is the transformation from conservative to entropy variables [6, 14]. Last five terms in Eq. 5 originate from weak imposition of the Dirichlet boundary conditions. In Eq. 5, $\boldsymbol{\tau}_B$ is a diagonal positive semi-definite matrix of stabilization parameters [54] (in this work a positive constant used in the definition of $\boldsymbol{\tau}_B$ is 4), and $\{\mathbf{A_n}\}_- = \{\mathbf{A}_i n_i\}_- = \mathbf{MT}\{\boldsymbol{\Lambda_n}\}_- \mathbf{T^{-1}M^{-1}}$ [53]. Operator $\{\cdot\}_-$ isolates the part of a matrix-valued argument corresponding to the eigenvalues with negative real parts. $\boldsymbol{\Lambda_n}$ is the diagonal matrix of the eigenvalues of $\mathbf{A_n}$ and $\mathbf{T}$ is the transformation matrix constructed using the eigenvectors as columns [53]. $\mathbf{M}$ is the Jacobian matrix $\partial \mathbf{U}/\partial \tilde{\mathbf{U}}$, where $\tilde{\mathbf{U}} = [\rho, \ \mathbf{u}^T, \ p]^T$, and defined as

$$\mathbf{M} = \begin{bmatrix} 1 & 0 & 0 & 0 & 0 \\ 0 & \rho & 0 & 0 & 0 \\ 0 & 0 & \rho & 0 & 0 \\ 0 & 0 & 0 & \rho & 0 \\ 0 & 0 & 0 & 0 & (\gamma-1)^{-1} \, e_{tot}/e \end{bmatrix}, \quad (8)$$

where γ is the adiabatic index and $e_{tot} = e + \mathbf{u} \cdot \mathbf{u}/2$ is the total energy.

Remark 1 We focus on the last term of Eq. 5 and consider inflow and wall boundary conditions. We set the inflow boundary conditions strongly on all the variables, which implies $\mathbf{W}^h = 0$ and $\mathbf{U}(\mathbf{Y}^h) = \mathbf{U}(\mathbf{Y}_G^h)$. As a result, this term does not contribute to the formulation. In the case of wall boundary conditions, we set the temperature strongly and velocity weakly. This results in $\mathbf{U}(\mathbf{Y}^h) - \mathbf{U}(\mathbf{Y}_G^h) = [0, \ \rho \, (\mathbf{u} - \mathbf{g}), \ \rho \, (\mathbf{u} \cdot \mathbf{u}/2 - \mathbf{g} \cdot \mathbf{g}/2)]^T$. In addition, $W_5{}^h = 0$. Because $\{\hat{\mathbf{A}}_\mathbf{n}\}_-$ is a fully populated matrix, the weak boundary condition terms will produce a contribution that has a mismatch in the momentum and kinetic energy density.

The semi-discrete formulation defined in Eq. 5 is integrated in time using the generalized-α method [3, 9, 20, 54] (in this work the generalized-α parameter $\rho_\infty = 0.5$). All simulations are done with a constant time step. The Newton–Raphson method is used to solve the resulting non-linear

system of equations. At each non-linear iteration, the linear system is solved through the Generalized Minimal Residual method (GMRES) [37]. The convergence criteria used for non-linear and linear solvers is the three orders of magnitude reduction in the norm of the residual.

3 Numerical results

In this section the numerical results for the compression corner, the cylinder and the Mars Pathfinder re-entry vehicle are presented. The results are compared with available experimental data and if no experimental data is available the results are compared with numerical tests from the literature.

3.1 Compression corner

The compression corner in hypersonic flows belongs to a category of cases associated with shock wave-boundary layer interaction (SWBLI) problems [2]. It is characterized by a flat plate section followed by an inclined section at a certain angle α. The flow physics is characterized by a primary shock wave downstream the corner and a separation region, the size of which varies depending on the Mach number and the angle α. The primary shock originates from the streamlines deflection due to the wedge angle α. The strong adverse pressure gradient due to the primary shock wave compression cause the flow to separate around the corner. A secondary shock wave forms because of the flow separation. The strength of the separation shock also depends on the Mach number and the angle α. The separation shock strengthens the primary shock, resulting in higher pressure and wall heat flux. The impingement of the primary shock on the boundary layer on the inclined section of the model creates a high pressure region that compresses the boundary layer, making it thinner, which generates high surface heat flux. Two compression corner cases are considered, one at $\alpha = 15°$ and the other one at $\alpha = 24°$. The flow for the compression corner at $\alpha = 15°$ remains attached and it does not separate at the corner, while a wide separation region is observed for the case at $\alpha = 24°$.

3.1.1 Compression corner at 15°

The compression corner at $\alpha = 15°$ is presented first. The free-stream is characterized by a Mach number $M_\infty = 14.1$ and a Reynolds number $Re_\infty = 2.6 \times 10^5$ [1/m]. At the inlet, $p_\infty = 10.02$ [Pa], $T_\infty = 72.22$ [K] and $u_\infty = 2401.9253$ [m/s] are imposed strongly. At the wall, the no-slip boundary conditions are imposed weakly, while the isothermal condition $T = 297.22$ [K] is only imposed strongly. At the outflow, as demonstrated in [38], the boundary integral is included for all flux terms, including the viscous and heat transfer contributions. The temperature
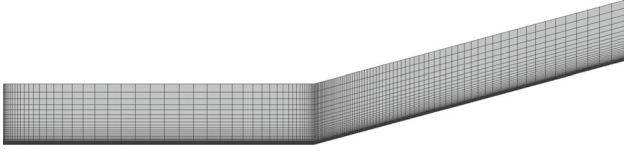
Fig. 1 Coarse computational grid for the compression corner at $\alpha = 15°$
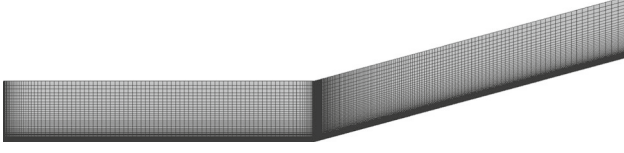
Fig. 2 Medium computational grid for the compression corner at $\alpha = 15°$
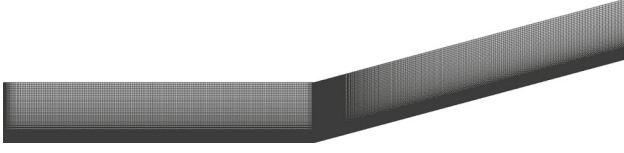
Fig. 3 Fine computational grid for the compression corner at $\alpha = 15°$

dependent viscosity is computed through the Sutherland law defined as:

$$\mu = \mu_{ref} \cdot \frac{T^{1.5}}{T + S}, \qquad (9)$$

where $\mu_{ref} = 1.458 \times 10^{-6}$ [Pa·s] and $S = 110.33$ [K]. The thermal conductivity is obtained from the Prandlt number definition as follows:

$$\lambda = \mu C_p / Pr, \qquad (10)$$

where $Pr = 0.72$ and the specific heat at constant pressure is constant and given as a function of the specific heat ratio $\gamma = 1.4$ and the universal gas constant R, as $C_p = \frac{\gamma R}{\gamma - 1}$.

Three computational structured grids are considered for this case. The elements are clustered close to the leading edge of the model and close to the wall. The coarse grid has 125 elements in the streamwise direction and 35 elements in the normal to the surface direction and is shown in Fig. 1. The medium grid is 250 by 70 elements and is shown in Fig. 2. The fine grid is 500 by 140 elements in the streamwise and wall normal directions respectively and is shown in Fig. 3. The grid convergence study is performed on non-dimensional coefficient for the surface heat flux defined as follows:

$$C_h = \frac{q}{\rho_\infty u_\infty (H_\infty - H_{wall})}, \qquad (11)$$

where H_∞ and H_{wall} is the total enthalpy at the inflow and the wall respectively. The simulations were done with a constant time step of 1×10^{-6} [s] until a steady-state solution is
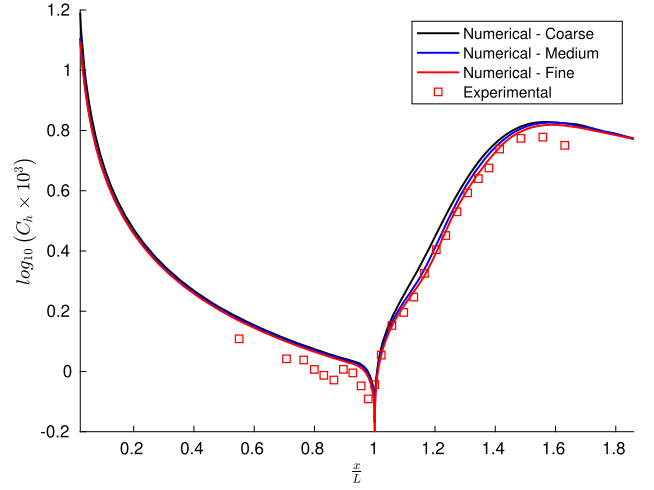
Fig. 4 Distribution of the surface heat flux coefficient C_h for the compression corner at $\alpha = 15°$
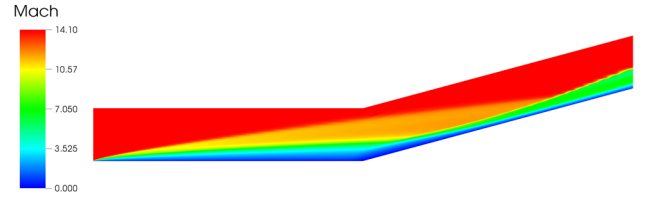
Fig. 5 Mach number contours for the compression corner at $\alpha = 15°$

obtained. The distribution of the surface heat transfer coefficient is illustrated in Fig. 4. The results agree quite well with the experiments data obtained by Holden [15] with slight overprediction of the heat flux in the flat plate section, but excellent agreement is obtained at the region where the boundary layer is thinned by the compression generated by the primary shock. Based on this study the medium mesh is selected to vizualize the flow topology and also study the 24° compression corner. The flow topology is shown in Fig. 5. No flow separation is observed as discussed earlier and smooth solution is obtained throughout the domain, showing the accuracy of the stabilization parameters and the discontinuity capturing term.

3.1.2 Compression corner at 24°

Next, the compression corner at $\alpha = 24°$ is investigated. The boundary conditions and fluid properties are similar to 15° case. As suggested by [36], the three-dimensional effects cannot be neglected and they strongly affect the prediction of the extent of the separation region. The medium computational grid from 15° case is used with 25 elements in the transverse direction and is shown in Fig. 6. The minimum element size at the wall-normal direction is 5×10^{-5} [m] and a constant time step of 1×10^{-6} [s] is used.
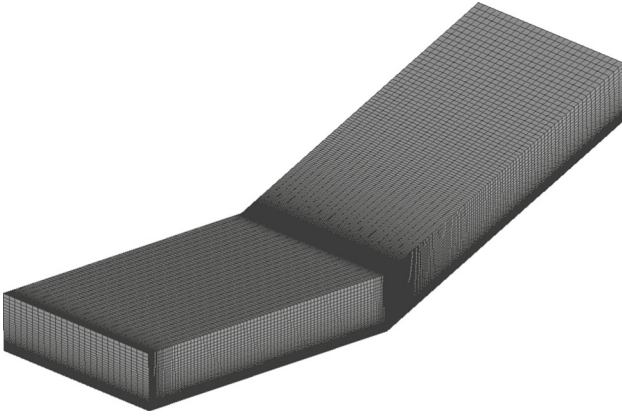
Fig. 6 Medium computational grid for the compression corner at $\alpha = 24°$
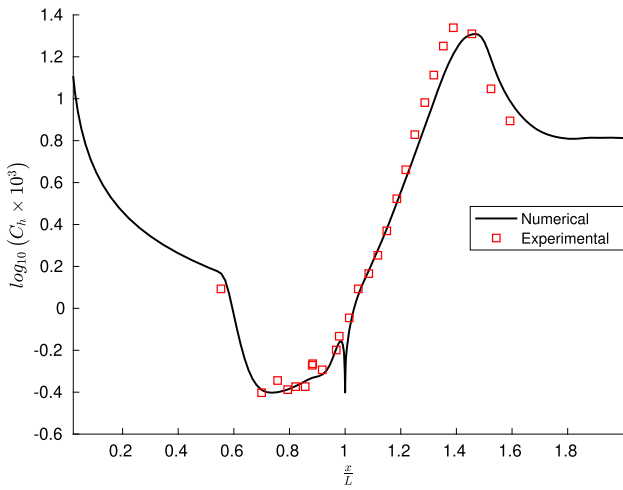
Fig. 7 Distribution of the surface heat flux coefficient C_h for the compression corner at $\alpha = 24°$
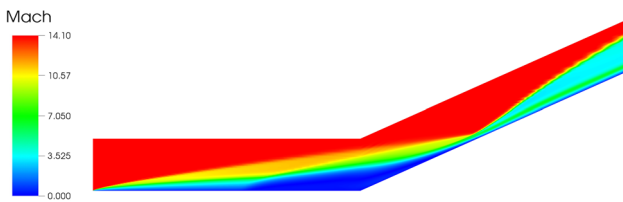
Fig. 8 Mach number contours for the compression corner at $\alpha = 24°$

The heat flux distribution is shown in Fig. 7 and in a good agreement with the experimental data [15], especially in the separation region. Only the slight underprediction of the peak heat flux can be observed further downstream. The flow topology can be observed in Fig. 8, showing a wide separation region around the corner of the model. The numerical solution accurately capture the impingment of the separation shock on the primary shock and the thinning of the boundary layer due to the high pressure.
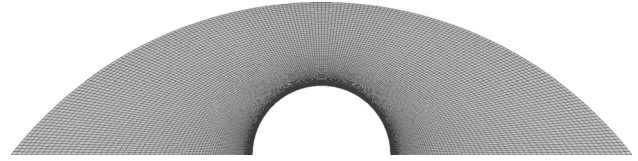
Fig. 9 Computational grid for the cylinder case

3.2 Flow over a 2D cylinder

In this section the laminar cylinder case immersed in a hypersonic flow is presented. This is a standard 2D benchmark case for hypersonic flows. The free-stream is defined by a Mach number $M_\infty = 17$ and a Reynolds number $Re_\infty = 7.52 \times 10^5$. The free-stream conditions at the inlet $p_\infty = 57.4\,[\text{Pa}]$, $T_\infty = 200\,[\text{K}]$, $u_\infty = 5000\,[\text{m/s}]$ are imposed strongly. The no-slip boundary condition is imposed weakly at the wall, while the isothermal condition $T_w = 500\,[\text{K}]$ is imposed strongly. At the outflow, as demonstrated in [38], the boundary integral is included for all flux terms, including the viscous and heat transfer contributions. The temperature dependent viscosity is calculated using the Sutherland law as in Eq. 9 and the thermal conductivity as in Eq. 10. For this case a structured computational grid is used and is shown in Fig. 9. The grid is characterized by 180 elements in the azimuthal direction and 140 elements in the radial direction. The elements are clustered towards the wall, where the smallest element size in a radial direction is $5 \times 10^{-5}\,[\text{m}]$. A constant time-step of $1 \times 10^{-6}\,[\text{s}]$ is used.

The flow field developed around the 1 [m] radius cylinder, is shown in Fig. 10. The bow shock developed around the cylinder, shows some oscillations towards the outlet boundary. These small oscillations are grid related, since the shock-grid alignment is progressively lost moving away from the stagnation region.

The distribution of the surface heat flux is shown in Fig. 11. The results obtained by the present formulation are compared to the numerical data obtained using LAURA code by Quattrochi [33]. The results slightly underpredict the data from Quattrochi in the region between the stagnation point and the bottom part of the cylinder, while the peak heat transfer
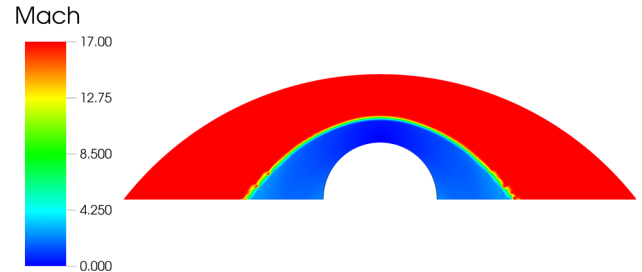
Fig. 10 Mach number contours for the cylinder case
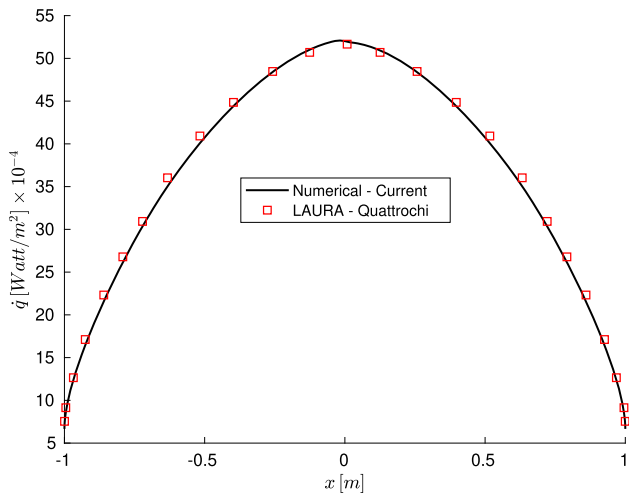
Fig. 11 Distribution of the surface heat flux for the cylinder case

Fig. 13 Cross-sectional slice of the Mach number contours for the Mars Pathfinder re-entry vehicle simulation

3.3 Mars Pathfinder re-entry vehicle

In this section the 3D Mars Pathfinder re-entry vehicle is analysed. A detailed numerical and experimental aerothermodynamics analysis of the re-entry vehicle in hypersonic regime, have been carried out in [16]. The geometry of this case is taken from the experimental model defined as $MP - 1$ in [16]. The computational grid is shown in Fig. 12. The grid is unstructured and contains a refinement section around the capsule. The resolution of the boundary layer grid is shown in Fig. 12b and it is characterized by 27 layers with the smallest element size in the wall-normal direction of 1.25×10^{-5} [m]. The free-stream is characterized by a Mach number $M_\infty = 10$ and a Reynolds number $Re_\infty = 3.187 \times 10^6$. The free-stream conditions imposed at the inlet strongly are $p_\infty = 130.5$ [Pa], $u_\infty = 1415$ [m/s], $T_\infty = 51.63$ [K]. The wall is isothermal at $T = 300$ [K], which is imposed strongly, and the no-slip boundary con-

predicted by the present formulation agrees quite well with the one obtained in [33].

dition is imposed weakly. At the outflow, as demonstrated in [38], the boundary integral is included for all flux terms, including the viscous and heat transfer contributions. The flow topology can be seen in Fig. 13. The flow field is mainly characterized by a bow shock in front of the body. Behind the vehicle two symmetric recirculation regions are observed. A shear layer develops between the post shock region and the recirculation region and an oblique shock wave develops downstream the vehicle on the sting.

The surface heat transfer distribution is shown in Fig. 14 as a function of the curvilinear coordinate S/R_b, where R_b is the vehicle radius. The results are compared to the experimental data obtained by Hollis for the Test 293 Run 007 [16]. The numerical results are in a good agreement with the experiment, mostly within the reported uncertainty, except for the location of the shock wave on the sting, where the results are slightly underpredicted. The slight overprediction of heat transfer in the front part of the vehicle, downstream the stagnation point, may be related to a coarser grid resolution at the shock location, with respect to the resolution right in front of the stagnation point.
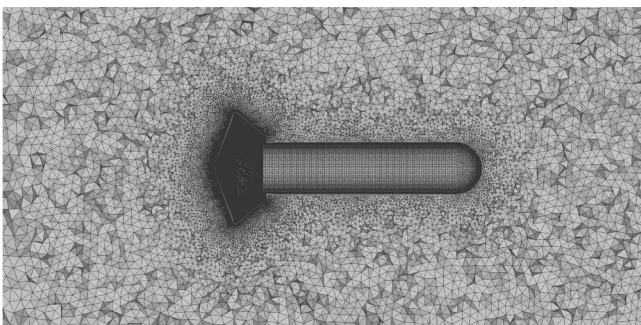
(a) Cross-sectional slice of the computational grid.
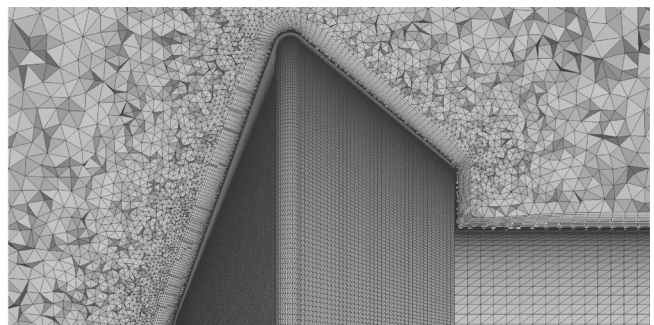
(b) Zoom on the boundary layer grid.

Fig. 12 Computational grid for the Mars Pathfinder re-entry vehicle
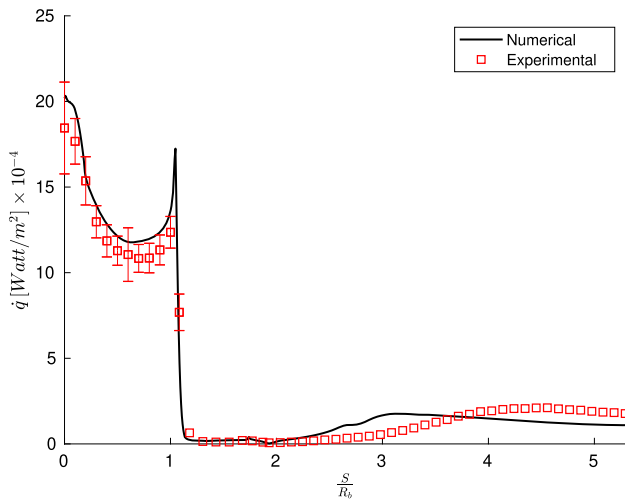
Fig. 14 Distribution of the surface heat transfer for the Mars Pathfinder re-entry vehicle simulation

4 Conclusion

The present work proposes the stabilized finite element formulation enhanced with a weak imposition of the no-slip boundary condition. The formulation is tested on the prediction of the surface heat flux for vaarious benchmark cases, including the compression corner at 15° and 24°, the 2D cylinder at Mach 17 and the 3D Mars Pathfinder re-entry vehicle. The numerical results are compared with the available experimental data and numerical data from in the literature. The overall good agreement is obtained showing the suitability of the stabilized formulation in predicting essential quantities such as the heat transfer in the context of hypersonic flows. The imposition of the no-slip boundary condition in a weak way provides a promising alternative to a classical imposition of the Dirichlet boundary condition. A further investigation, however, is needed. Particular attention should be given to the weak imposition of the isothermal condition at the wall. This will be the next step, where a full comparison between the strongly imposed wall boundary conditions and the weakly imposed boundary conditions will be carried out.

References

1. Almeida RC, Galeão AC (1996) An adaptive Petrov–Galerkin formulation for the compressible Euler and Navier–Stokes equations. Comput Methods Appl Mech Eng 129(1):157–176
2. Babinsky H, Harvey JK (2011) Shock wave-boundary-layer interactions. Cambridge University Press
3. Bazilevs Yuri, Kamensky David, Moutsanidis Georgios, Shende Shaunak (2020) Residual-based shock capturing in solids. Comput Methods Appl Mech Eng 358:112638
4. Bazilevs Y, Takizawa K, Wu MCH, Kuraishi T, Avsar R, Xu Z, Tezduyar TE (2021) Gas turbine computational flow and structure analysis with isogeometric discretization and a complex-geometry mesh generation method. Comput Mech 67:57–84
5. Brooks AN, Hughes TJR (1982) Streamline upwind Petrov–Galerkin formulations for convection dominated flows with particular emphasis on the incompressible Navier–Stokes equations. Comput Methods Appl Mech Eng 32:199–259
6. Chalot F, Hughes TJR, Shakib F (1990) Symmetrization of conservation laws with entropy for high-temperature hypersonic computations. Comput Syst Eng 1(2–4):495–521
7. Ching EJ, Lv Y, Gnoffo P, Barnhardt M, Ihme M (2019) Shock capturing for discontinuous Galerkin methods with application to predicting heat transfer in hypersonic flows. J Comput Phys 376:54–75
8. Ching E, Lv Y, Ihme M (2017) Development of discontinuous Galerkin method for hypersonic heating prediction. In: 55th AIAA aerospace sciences meeting
9. Codoni D, Moutsanidis G, Hsu MC, Bazilevs Y, Johansen C, Korobenko A (2021) Stabilized methods for high-speed compressible flows: toward hypersonic simulations. Comput Mech 67:785–809
10. Codoni D, Johansen C, Korobenko A (2022) A streamline-upwind Petrov–Galerkin formulation for the analysis of hypersonic flows in thermal non-equilibrium. Comput Methods Appl Mech Eng 398:115185
11. Dick E (2009) Computational fluid dynamics, chapter 10. Springer, pp 235–274
12. Gibbons NN, Damm KA, Jacobs PA, Gollan RJ (2023) Eilmer: an open-source multi-physics hypersonic flow solver. Comput Phys Commun 282
13. Hauke G (2001) Simple stabilizing matrices for the computation of compressible flows in primitive variables. Comput Methods Appl Mech Eng 190:6881–6893
14. Hauke G, Hughes TJR (1998) A comparative study of different sets of variables for solving compressible and incompressible flows. Comput Methods Appl Mech Eng 153:1–44
15. Holden MS (1970) Theoretical and experimental studies of the shock wave-boundary layer interaction on compression surfaces in hypersonic flow. Technical report, Cornell Aeronautical Lab Inc, Buffalo, NY
16. Hollis BR (1996) Experimental and computational aerothermodynamics of a Mars entry vehicle. North Carolina State University
17. Hughes TJR, Tezduyar TE (1984) Finite element methods for first-order hyperbolic systems with particular emphasis on the compressible Euler equations. Comput Methods Appl Mech Eng 45:217–284
18. Hughes TJR, Mallet M, Mizukami A (1986) A new finite element formulation for computational fluid dynamics: II beyond SUPG. Comput Methods Appl Mech Eng 54:341–355
19. Hughes TJR, Scovazzi G, Tezduyar TE (2010) Stabilized methods for compressible flows. J Sci Comput 43:343–368
20. Jansen KE, Whiting CH, Hulbert GM (2000) A generalized-alpha method for integrating the filtered Navier–Stokes equations with a stabilized finite element method. Comput Methods Appl Mech Eng 190:305–319
21. Kanai T, Takizawa K, Tezduyar TE, Tanaka T, Hartmann A (2019) Compressible-flow geometric-porosity modeling and spacecraft parachute computation with isogeometric discretization. Comput Mech 63:301–321

22. Kirk BS, Stogner RH, Bauman PT, Oliver TA (2014) Modeling hypersonic entry with the fully-implicit Navier–Stokes (FIN-S) stabilized finite element flow solver. Comput Fluids 92:281–292

23. Kitamura K (2013) A further survey of shock capturing methods on hypersonic heating issues. In: 21st AIAA computational fluid dynamics conference

24. Kitamura K, Shima E (2013) Towards shock-stable and accurate hypersonic heating computations: a new pressure flux for AUSM-family schemes. J Comput Phys 245:62–83

25. Kitamura K, Shima E, Nakamura Y, Roe PL (2010) Evaluation of Euler fluxes for hypersonic heating computations. AIAA J 48(4):763–776

26. Kozak N, Rajanna MR, Wu MCH, Murugan M, Bravo L, Ghoshal A, Hsu MC, Bazilevs Y (2020) Optimizing gas turbine performance using the surrogate management framework and high-fidelity flow modeling. Energies

27. Le Beau GJ, Tezduyar TE (1991) Finite element computation of compressible flows with the SUPG formulation. Am Soc Mech Eng Fluids Eng Div (Publ) FED 123:21–27

28. Le Beau GJ, Ray SE, Aliabadi SK, Tezduyar TE (1993) SUPG finite element computation of compressible flows with entropy and conservation variables formulations. Comput Methods Appl Mech Eng 104:397–422

29. Liu F, Bao L (2023) Peak heat flux prediction of hypersonic flow over compression ramp under vibrationally excited free-stream condition. Phys Fluids 35(1):016120

30. Lu J, Li J, Song Z, Zhang W, Yan C (2022) Uncertainty and sensitivity analysis of heat transfer in hypersonic three-dimensional shock waves/turbulent boundary layer interaction flows. Aerosp Sci Technol 123:107447

31. Nastac G, Tramel RW, Nielsen EJ (2022) Improved heat transfer prediction for high-speed flows over blunt bodies using adaptive mixed-element unstructured grids. In: AIAA SCITECH 2022 forum

32. Pirbastami S (2023) LES simulation of hypersonic flow over hollow cylinder flare. In: AIAA SCITECH 2023 forum

33. Quattrochi DJ (2006) Hypersonic heat transfer and anisotropic visualization with a higher order discontinuous Galerkin finite element method. Ph.D. Thesis, Massachusetts Institute of Technology

34. Rajanna MR, Johnson EL, Codoni D, Korobenko A, Bazilevs Y, Liu N, Lua J, Phan ND, Hsu MC (2022) Finite element simulation and validation for aerospace applications: Stabilized methods, weak Dirichlet boundary conditions, and discontinuity capturing for compressible flows. In: AIAA SCITECH 2022 forum

35. Rajanna MR, Johnson EL, Codoni D, Korobenko A, Bazilevs Y, Liu N, Lua J, Phan N, Hsu MC (2022) Finite element methodology for modeling aircraft aerodynamics: development, simulation, and validation. Comput Mech 70:549–563

36. Rudy DH, Thomas JL, Kumar A, Gnoffo PA, Chakravarthy SR (1991) Computation of laminar hypersonic compression-corner flows. AIAA J 29(7):1108–1113

37. Saad Y, Schultz MH (1986) GMRES: a generalized minimal residual algorithm for solving nonsymmetric linear systems. SIAM J Sci Stat Comput 7(3)

38. Shakib F, Hughes TJR, Johan Z (1991) A new finite element formulation for a computational fluid dyamics: X. The compressible Euler and Navier–Stokes equations. Comput Methods Appl Mech Eng 89:141–219

39. Sturek WB, Ray S, Aliabadi S, Waters C, Tezduyar TE (1997) Parallel finite element computation of missile aerodynamics. Int J Numer Methods Fluids 24:1417–1432

40. Sziroczak D, Smith H (2016) A review of design issues specific to hypersonic flight vehicles. Prog Aerosp Sci 84:1–28

41. Takizawa K, Tezduyar TE, Kanai T (2017) Porosity models and computational methods for compressible-flow aerodynamics of parachutes with geometric porosity. Math Models Methods Appl Sci 27:771–806

42. Takizawa K, Tezduyar TE, Otoguro Y (2018) Stabilization and discontinuity-capturing parameters for space–time flow computations with finite element and isogeometric discretizations. Comput Mech 62:1169–1186

43. Tezduyar TE, Hughes TJR (1982) Development of time-accurate finite element techniques for first-order hyperbolic systems with particular emphasis on the compressible Euler equations. NASA Technical Report NASA-CR-204772

44. Tezduyar TE, Hughes TJR (1982) Development of time-accurate finite element techniques for first-order hyperbolic systems with particular emphasis on the compressible Euler equations. Technical report, NASA-CR-204772, Division of Applied Mechanics Department of Mechanical Engineering, Stanford University, Stanford, CA 94305

45. Tezduyar TE, Hughes TJR (1983) Finite element formulations for convection dominated flows with particular emphasis on the compressible Euler equations. In: 21st Aerospace sciences meeting

46. Tezduyar TE, Park YJ (1986) Discontinuity capturing finite element formulations for nonlinear convection–diffusion–reaction equations. Comput Methods Appl Mech Eng 59:307–325

47. Tezduyar TE, Senga M (2006) Stabilization and shock-capturing parameters in SUPG formulation of compressible flows. Comput Methods Appl Mech Eng 195:1621–1632

48. Tezduyar TE, Senga M (2007) SUPG finite element computation of inviscid supersonic flows with YZβ shock-capturing. Comput Fluids 36:147–159

49. Tezduyar T, Aliabadi S, Behr M, Johnson A, Mittal S (1993) Parallel finite-element computation of 3D flows. Computer 26(10):27–36

50. Tezduyar TE, Aliabadi SK, Behr M, Mittal S (1994) Massively parallel finite element simulation of compressible and incompressible flows. Comput Methods Appl Mech Eng 119:157–177

51. Tezduyar T, Aliabadi S, Behr M, Johnson A, Kalro V, Litke M (1996) Flow simulation and high performance computing. Comput Mech 18:397–412

52. Tezduyar TE, Senga M, Vicker D (2006) Computation of inviscid supersonic flows around cylinders and spheres with the SUPG formulation and YZβ shock-capturing. Comput Mech 38:469–481

53. Warming RF, Beam RM, Hyett BJ (1975) Diagonalization and simultaneous symmetrization of the gas-dynamic matrices. Math Comput 29(132):1037–1045

54. Xu F, Moutsanidis G, Kamensky D, Hsu MC, Murugan M, Ghoshal A, Bazilevs Y (2017) Compressible flows on moving domains: stabilized methods, weakly enforced essential boundary conditions, sliding interfaces, and application to gas-turbine modeling. Comput Fluids 158:201–220

55. Xu F, Bazilevs Y, Hsu MC (2019) Immersogeometric analysis of compressible flows with application to aerodynamic simulation of rotorcraft. Math Models Methods Appl Sci 29(5):905–938